

Rydberg Atomic Receivers for Multi-Band Communications and Sensing

Mingyao Cui, Qunsong Zeng, Zhanwei Wang, and Kaibin Huang, *Fellow, IEEE*

Abstract—Harnessing multi-level electron transitions, Rydberg Atomic REceivers (RAREs) can detect wireless signals across a wide range of frequency bands, from Megahertz to Terahertz, enabling multi-band communications and sensing (CommunSense). Current research on multi-band RAREs primarily focuses on experimental demonstrations, lacking a tractable model to mathematically characterize their mechanisms. This issue leaves the multi-band RARE as a black box, posing challenges in its practical CommunSense applications. To fill in this gap, this paper investigates the underlying mechanism of multi-band RAREs and explores their optimal performance. For the first time, the closed-form expression of the transfer function of a multi-band RARE is derived by solving the quantum response of Rydberg atoms excited by multi-band signals. The function reveals that a multi-band RARE simultaneously serves as both a *multi-band atomic mixer* for down-converting multi-band signals and a *multi-band atomic amplifier* that reflects its sensitivity to each band. Further analysis of the atomic amplifier unveils that the gain factor at each frequency band can be decoupled into a *global gain* term and a *Rabi attention* term. The former determines the overall sensitivity of a RARE to all frequency bands of wireless signals. The latter influences the allocation of the overall sensitivity to each frequency band, representing a unique attention mechanism of multi-band RAREs. The optimal design of the global gain is provided to maximize the overall sensitivity of multi-band RAREs. Subsequently, the optimal Rabi attentions are also derived to maximize the practical multi-band CommunSense performance. Numerical results confirm the effectiveness of the derived transfer function and the superiority of multi-band RAREs.

Index Terms—Rydberg atomic receivers, wireless communications, wireless sensing, multi-band signal detection.

I. INTRODUCTION

The precise measurement of radio-frequency (RF) signals is fundamental to the digital age, serving as a core operation in wireless communications, remote sensing, e-health, and radar systems. Emerging from the domain of quantum sensing, the Rydberg Atomic REceiver (RARE) has recently been introduced as a new concept in high-precision wireless detection by exploiting the quantum properties of Rydberg atoms [1]–[6]. Specifically, Rydberg atoms are highly excited atoms wherein one or more electrons have transitioned from their ground-state energy level to an excited energy state. Due to their large transition dipole moments, Rydberg atoms can strongly interact with incident RF signals, triggering electron transitions between resonant energy levels [4]. Capitalizing on these transitions, RAREs can capture the amplitude, frequency, phase, and polarization of RF signals with unparalleled precision. Consequently, RAREs have the potential to complement or

even replace traditional RF receivers in the next-generation wireless communications and sensing (CommunSense) systems [7]–[14].

RAREs offer two major advantages over classical receivers: extremely high sensitivity and a wide range of detectable frequency bands. Classical receivers, comprising metallic antennas and RF front-end circuitry, are fundamentally constrained by Johnson-Nyquist noise that arises from the random thermal motion of free electrons [15]. In contrast, the quantum process governing RAREs—electron transition between Rydberg states—is inherently immune to thermal noise. This immunity enables RAREs to achieve exceptional sensitivity to RF signals, potentially 1~2 orders of magnitude higher than that of traditional counterparts as demonstrated in [16], [17]. Additionally, conventional metallic antennas require physical dimensions comparable to the carrier wavelength to efficiently couple with incident RF signals. As a result, their detectable frequency ranges are intrinsically limited by their geometric sizes [18], [19]. In contrast, by utilizing electron transitions between numerous energy levels, a single RARE can simultaneously detect multiple distinct frequency bands, ranging from Megahertz (MHz) to Terahertz (THz), without any change of the hardware [7]. This distinctive feature underpins the development of integrated full-frequency wireless CommunSense platforms, unifying sub-6G, midband, millimeter wave (mmWave), and THz bands into a single receiver architecture. This paper exploits the RAREs’ multi-band detection capability to reshape wireless CommunSense systems.

Existing studies have experimentally validated the concurrent multi-band CommunSense capabilities of RAREs. The initial demonstration of dual-band communications was reported in [20], where two species of Rydberg alkali atoms—rubidium and cesium—each with distinct energy-level structures, were mixed in a single vapor cell. This configuration enabled the simultaneous detection of amplitude-modulated (AM) signals at 19.626 GHz and frequency-modulated (FM) signals at 20.644 GHz. Subsequent research demonstrated that leveraging the electron transitions between different energy levels within a single atom species, (e.g., cesium), is sufficient to capture multiple frequency bands, which has become a common practice [21]. In particular, the concurrent measurement of frequency bands at 1.72, 12.11, 27.42, 65.11, and 115.75 GHz has been reported in [22]. It utilizes the technology of *quantum heterodyne sensing*, which introduces external reference signals for assisting signal detection, to excite electron transitions between chosen energy levels, $56D_{5/2}$, $57P_{3/2}$, $54F_{7/2}$, $52F_{7/2}$, and $59P_{3/2}$. Further advances include chip-integrated RAREs for dual-band operation at 300 MHz and 24 GHz [23], and a cascaded orbital angular-momentum transitions to enable coverage from 128 MHz to

The authors are with Department of Electrical and Electronic Engineering, The University of Hong Kong, Hong Kong (Emails: {mycui, qszeng, zhanwei}@eee.hku.hk, huangkb@hku.hk). Corresponding authors: Q. Zeng; K. Huang.

0.61 THz [24]. Additionally, experiments have also revealed a sensitivity tradeoff of the multi-band RARE [25]. Specifically, its sensitivities to different frequency bands can influence each other—an increase in sensitivity at one band might result in decreased sensitivity at other bands. Some recent studies have also explored the applications of multi-band RAREs, including the frequency-hopping communication and angles-of-arrival (AoAs) sensing [26], [27].

RARE enabled multi-band CommunSense is still in its infancy. Currently, there exists no tractable models to mathematically characterize the working mechanisms of multi-band RAREs. Prior studies largely in the physics community have predominantly emphasized experimental verifications [20]–[26]. In the existing literature, only the work in [27] makes an initial attempt to establish a signal model for multi-band RAREs. However, the derivation directly adopts the conventional single-band RARE framework, which might be over-simplified as it neglects some delicate but important characteristics of multi-band RAREs. The lack of a tractable theory renders the multi-band RARE as a black box, hindering rigorous analysis of their quantum phenomena (e.g., the mentioned sensitivity tradeoff) and performance optimization.

To fill in this knowledge gap, we make an attempt to theoretically characterize the underlying mechanisms of multi-band RAREs and apply the results to optimize their performance in wireless CommunSense systems. We leverage multi-level electron transitions in Rydberg atoms to enable simultaneous multi-band signal reception, augmented by quantum heterodyne sensing to facilitate signal detection. It is worth emphasizing that the considered multi-band RARE architecture enables detection of disjoint bands while the conventional orthogonal frequency division multiplexing (OFDM) systems are confined to a single contiguous frequency block (e.g., a 100 MHz channel at 3.5 GHz in 5G standard [28]). The key contributions and findings of our work are summarized as follows.

- **Theoretical framework of multi-band RAREs:** We develop a theoretical framework to characterize the operational mechanisms underlying realistic multi-band RAREs. By solving the Lindblad master equation governing their operations, a closed-form expression is derived for the quantum response of Rydberg atoms excited by multi-band RF signals. This solution quantifies the transfer function of a multi-band RARE, revealing its dual role as a *multi-band atomic mixer* and a *multi-band atomic amplifier*. Specifically, each wireless signal undergoes frequency down-conversion to the intermediate frequency (IF) via the transition frequency of its coupled energy-level pair. The IF component is then amplified by a *band-specific gain factor*. Our analysis reveals that this amplification gain factor directly determines the sensitivity of the RARE.
- **Sensitivity maximization of multi-band RAREs:** Based on the preceding framework, we maximize the sensitivities of a RARE across all frequency bands by tuning the Rabi frequencies (electron transition strengths) of external reference signals in quantum heterodyne sensing. This problem is complex due to the aforementioned

mutual coupling among multi-band sensitivities. To solve the problem, we prove that each gain factor (sensitivity) associated with an individual band can be decomposed into a *global gain* term (common to all bands) and a band-specific *Rabi attention* term. The former, which measures the overall sensitivity to all bands, depends solely on the sum-square of Rabi frequencies across all bands, referred to as the *Rabi sum-square*. The maximization of the RARE overall sensitivity can be achieved by optimizing this Rabi sum-square, for which the globally optimal solution is derived in closed form. On the other hand, the Rabi attentions characterize the distribution of Rabi sum-square over all frequency bands, which determine the allocation of overall sensitivity to each band. These Rabi attentions represent a unique attention mechanism of multi-band RAREs, providing additional degrees-of-freedom for optimization according to a downstream CommunSense metric.

- **CommunSense applications of multi-band RAREs:** Last, we apply the preceding results to performance optimization of the systems supporting multi-band communications and multi-granularity sensing. Their performances are evaluated using the metrics of spectral efficiency (SE) for communications and normalized Cramér-Rao lower bound (NCRLB) for sensing, both averaged across frequency bands. We derive the optimal design of Rabi attentions for each of these systems. Numerical experiments validate the superiority of a multi-band RARE over the classic receivers and the existing single-band RARE in these CommunSense applications.

The remainder of the paper is organized as follows. Section II presents the system model. The theoretical foundation of the multi-band RARE is established in Section III. The maximal sensitivity of a multi-band RARE is derived by optimizing the Rabi sum-square in Section IV. Section V elaborates on the applications of multi-band RARE in CommunSense systems and the associated optimal Rabi attention design. Numerical experiments are conducted in Section VI, and conclusions are drawn in Section VII.

II. SYSTEM MODEL

Consider the multi-band RARE system as illustrated in Fig. 1 (a). Multi-band signals spanning the frequency range from sub-6G to THz are simultaneously detected to offer diverse CommunSense services. For classical receivers, measuring these signals necessitates multiple antennas and RF front-end circuits due to the largely separated frequency bands [19], [29]. However, a single RARE is sufficient to capture them by exploiting the multi-level electron transitions as depicted in Fig. 1 (b). Relevant models are described in the sub-sections.

A. Incident Multi-Band Signal Model

The incident multi-band signal consists of N disjoint frequency bands, where the band spacings can extend up to tens of GHz, giving that

$$E_{\text{RF}}(t) = \sum_{n=1}^N E_{\text{RF},n}(t). \quad (1)$$

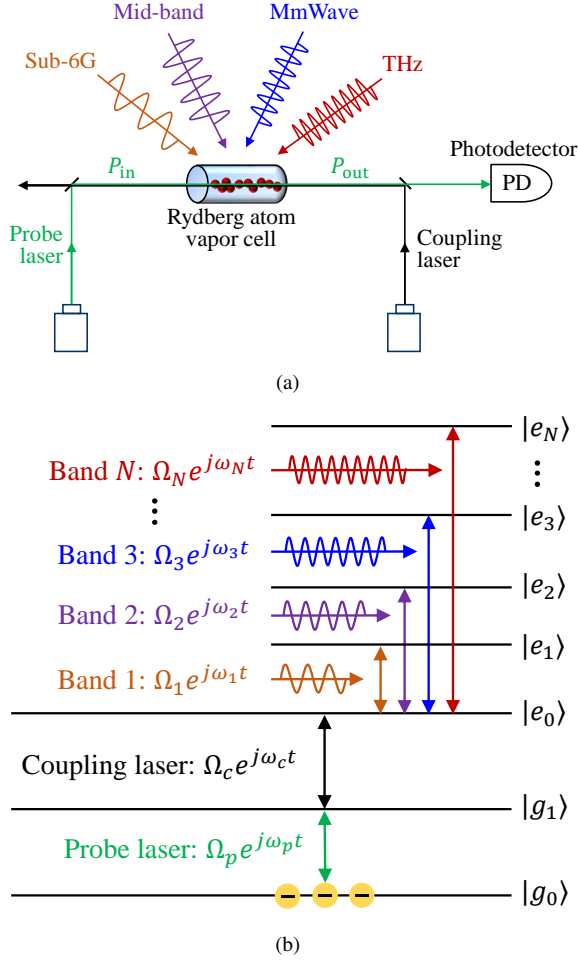


Figure 1. (a) The architecture of a multi-band RARE. (b) The multi-level electron transitions for measuring multi-band signals.

Here, $E_{\text{RF},n}(t)$ represents the incident RF signal at band n formulated as

$$E_{\text{RF},n}(t) = \text{Re}\{E_n(t)e^{j\omega_n t}\}, \quad (2)$$

where ω_n denotes the angular frequency of band n and $E_n(t) \in \mathbb{C}$ the baseband component. The occupied bandwidth of each RF signal $E_{\text{RF},n}(t)$ is denoted as B_n .

Existing multi-band RARE systems popularly employ the quantum heterodyne sensing technique to facilitate signal detection [22]. This technique introduces external local oscillators (LOs), also known as reference sources, to generate reference signals that match the target wireless frequencies, $\omega_n, \forall n$. Then, the composite baseband signal, $E_n(t)$, consists of two parts: the LO-generated reference signal, denoted as $E_{r,n} \in \mathbb{C}$, and the data signal to be detected, denoted as $E_{s,n} \in \mathbb{C}$. Besides, to enable phase detection, a slight frequency offset, δ_n , between the reference and data signals is usually introduced, serving as the IF component. Without loss of generality, the IFs are configured in an ascending order $\delta_1 < \delta_2 < \dots < \delta_N$. As a result, the overall baseband signal $E_n(t)$ can be written as

$$E_n(t) = E_{r,n} + E_{s,n}e^{j\delta_n t}. \quad (3)$$

In practice, the reference signal $E_{r,n}$ is known to the RARE. The CommunSense information to be recovered are embedded within the data signal $E_{s,n}$, as elaborated below.

- *Communication signal*: Quadrature amplitude modulation (QAM) symbols are transmitted from N heterogeneous devices operating at distinct frequency bands. Let $s_n \in \mathbb{S}_n$ be the QAM symbol from the n -th device, normalized such that $\mathbb{E}[|s_n|^2] = 1$, where \mathbb{S}_n denotes the QAM constellation set. Then, the baseband data signal, $E_{s,n}$, for communication service is modeled as

$$E_{s,n} = h_n \sqrt{P_{t,n}} s_n, \quad (4)$$

where $h_n \in \mathbb{C}$ is the flat-fading channel coefficient (assumed known via channel estimation), $\sqrt{P_{t,n}}$ is the transmit power at the n -th band. The multi-path effect is neglected due to the narrow bandwidth B_n of each band.

- *Sensing signal*: As the operating frequency ω increases, a minute target displacement d will induce a significant phase shift $\frac{\omega d}{c}$ to the RF signal, enhancing sensing granularity. By simultaneously detecting N frequency bands, multi-band RAREs achieve multi-scale sensing from coarse (e.g., hand tracking) to fine (e.g., finger tracking) resolutions. Specifically, at band n , the sensing target undergoes a slight displacement, d_n , which introduces an additional phase, $\frac{(\omega_n + \delta_n)}{c} d_n$, to the sensing signal, $\text{Re}\{E_{s,n}e^{j(\omega_n + \delta_n)t}\}$. Thus, $E_{s,n}$ is formulated as

$$E_{s,n} = h_n \sqrt{P_{t,n}} e^{j\frac{(\omega_n + \delta_n)}{c} d_n} \stackrel{(a)}{\approx} h_n \sqrt{P_{t,n}} e^{j\frac{\omega_n}{c} d_n}, \quad (5)$$

where the approximation (a) holds because $\omega_n \gg \delta_n$. To avoid phase ambiguity, displacements are constrained to $d_n \in \left[-\frac{\pi c}{\omega_n}, \frac{\pi c}{\omega_n}\right]$ [8], [10].

B. Multi-Level Electron Transition Model

As depicted in Fig. 1, a RARE utilizes the multi-level electron transitions of Rydberg atoms to interact with the multi-band signal, $E_{\text{RF}}(t)$. This interaction changes the quantum states of Rydberg atoms, resulting in variations in the absorption rate of the atomic ensemble to an incoming laser. By propagating a probe laser through these atoms and then monitoring the output probe-laser power using a photodetector (PD), the quantum state can be read out. This facilitates the detection of multi-band signals, $\{E_{s,n}\}$, and the recovery of multi-band CommunSense information, $\{s_n\}$ and $\{d_n\}$. The above physical processes are elaborated below.

1) *Quantum state*: In this system, a probe laser and a coupling laser propagate in opposite directions through a vapor cell filled with alkali atoms to prepare Rydberg atoms. As shown in Fig. 1(b), the probe laser excites electrons to jump from the ground state, denoted as $|g_0\rangle$, to a lowly excited state, denoted as $|g_1\rangle$. The coupling laser further triggers the electron transition from $|g_1\rangle$ to an initial Rydberg state, $|e_0\rangle$, thereby creating Rydberg atoms. These atoms interact with each frequency band of the incident signal, say band n , via the electron transition $|e_0\rangle \rightarrow |e_n\rangle, n \in \{1, 2, \dots, N\}$, respectively. As a result, the quantum response of each Rydberg atom

is characterized by an $(N + 3)$ -level system. The associated quantum state is thus an $(N + 3) \times (N + 3)$ Hermitian matrix

$$\rho = \begin{bmatrix} \rho_{11} & \rho_{12} & \cdots & \rho_{1,N+3} \\ \rho_{21} & \rho_{22} & \cdots & \rho_{2,N+3} \\ \vdots & \vdots & \ddots & \vdots \\ \rho_{N+3,1} & \rho_{N+3,2} & \cdots & \rho_{N+3,N+3} \end{bmatrix}, \quad (6)$$

satisfying $\text{Tr}\{\rho\} = 1$ and $\rho \succeq 0$.

2) *Hamiltonian operator*: The Hamiltonian operator governs electron transitions. Specifically, we define $\mu_{g_0g_1}$, $\mu_{g_1e_0}$, and μ_n , $\forall n \in \{1, \dots, N\}$ as the transition dipole moments associated with the electron transitions, $|g_0\rangle \rightarrow |g_1\rangle$, $|g_1\rangle \rightarrow |e_0\rangle$, and $|e_0\rangle \rightarrow |e_n\rangle$, $\forall n$, respectively. Let $\omega_{g_0g_1}$, $\omega_{g_1e_0}$, and $\omega_{e_0e_n}$, $\forall n$ be the transition frequencies of these electron transitions. We suppose that the amplitude and frequency of probe laser (coupling laser) are fixed as E_p (E_c) and ω_p (ω_c), respectively. Moreover, the resonant cases for all electron transitions are considered, meaning that $\omega_p = \omega_{g_0g_1}$, $\omega_c = \omega_{g_1e_0}$, and $\omega_n = \omega_{e_0e_n}$, $\forall n \in \{1, 2, \dots, N\}$. Following these definitions, the Rabi frequencies of the probe and coupling lasers, which quantify the strength of the interaction between the signal and the electron transition, can be represented as [30]

$$\Omega_p = \frac{\mu_{g_0g_1}}{\hbar} |E_p| \quad \text{and} \quad \Omega_c = \frac{\mu_{g_1e_0}}{\hbar} |E_c|, \quad (7)$$

respectively, where \hbar is the reduced Plank constant. Furthermore, the Rabi frequency pertaining to each RF signal component, $E_{\text{RF},n}(t)$, $\forall n \in \{1, 2, \dots, N\}$, is given as

$$\begin{aligned} \Omega_n &= \frac{\mu_n}{\hbar} |E_n(t)| = \frac{\mu_n}{\hbar} |E_{r,n} + E_{s,n} e^{j\delta_n t}|, \\ &\triangleq |\Omega_{r,n} + \Omega_{s,n} e^{j(\delta_n t + \varphi_n)}|. \end{aligned} \quad (8)$$

The variable ($\varphi_n = \angle E_{s,n} - \angle E_{r,n}$) denotes the phase difference between $E_{s,n}$ and $E_{r,n}$. Besides, $\Omega_{r,n} \triangleq \frac{\mu_n}{\hbar} |E_{r,n}|$ and $\Omega_{s,n} \triangleq \frac{\mu_n}{\hbar} |E_{s,n}|$ refer to the Rabi frequencies of the reference and data signals, respectively. For convenience in future use, we define the Rabi frequency vectors of the reference signals, data signals, and overall signals as $\Omega_r = [\Omega_{r,1}, \dots, \Omega_{r,N}]^T$, $\Omega_s = [\Omega_{s,1}, \dots, \Omega_{s,N}]^T$, and $\Omega = [\Omega_1, \dots, \Omega_N]^T$. As a result, the Hamiltonian operator for this $(N + 3)$ -level quantum system is represented as

$$\mathbf{H} = \frac{\hbar}{2} \begin{bmatrix} 0 & \Omega_p & 0 & 0 & \cdots & 0 \\ \Omega_p & 0 & \Omega_c & 0 & \cdots & 0 \\ 0 & \Omega_c & 0 & \Omega_1 & \cdots & \Omega_N \\ 0 & 0 & \Omega_1 & 0 & \cdots & 0 \\ \vdots & \vdots & \vdots & \vdots & \ddots & \vdots \\ 0 & 0 & \Omega_N & 0 & \cdots & 0 \end{bmatrix}, \quad (9)$$

which encompasses the Rabi frequencies of all external signals, Ω_p , Ω_c , and Ω_n , $\forall n$.

3) *Lindblad master equation*: The Hamiltonian operator, \mathbf{H} , drives the quantum state, ρ , to evolve over time, during which the Rabi frequencies are encoded into the quantum state. To be specific, the evolution follows the Lindblad master equation [31]

$$\frac{\partial \rho}{\partial t} = \frac{j}{\hbar} [\rho, \mathbf{H}] + \mathcal{L}, \quad (10)$$

where $[\rho, \mathbf{H}] \triangleq \rho \mathbf{H} - \mathbf{H} \rho$ represents the commutator between ρ and \mathbf{H} . The operator \mathcal{L} characterizes the noncoherent relaxation of the system, which is given in (11). Here, $\gamma_{ij} = (\gamma_i + \gamma_j)$, where γ_i ($i \in \{2, 3, \dots, N + 3\}$) refers to the decay rate of each energy level. In practice, the decay rate γ_2 is greater than γ_i ($i \in \{3, \dots, N + 3\}$) by orders of magnitude [31]. Thus, (11) is usually simplified to

$$\mathcal{L} = -\frac{\gamma_2}{2} \begin{bmatrix} -2\rho_{22} & \rho_{12} & 0 & 0 & \cdots & 0 \\ \rho_{21} & 2\rho_{22} & \rho_{23} & \rho_{24} & \cdots & \rho_{2,N+3} \\ 0 & \rho_{32} & 0 & 0 & \cdots & 0 \\ 0 & \rho_{42} & 0 & 0 & \cdots & 0 \\ \vdots & \vdots & \vdots & \vdots & \ddots & \vdots \\ 0 & \rho_{N+3,2} & 0 & 0 & \cdots & 0 \end{bmatrix},$$

for ease of analysis [31], [32].

4) *Measured quantum state*: The evolved quantum states are measured by a PD, which monitors the power loss of the probe laser when passing through the vapor cell. Specifically, let P_{in} be the input power of probe laser. According to the adiabatic approximation, the power of probe laser coming out of the vapor cell, denoted as $\mathcal{P}(\Omega)$, exponentially decays with the steady-state solution of ρ_{12} (the $(1, 2)$ -th entry of ρ) [31]

$$\mathcal{P}(\Omega) = P_{\text{in}} \exp(-C_0 \text{Im}\{\rho_{12}\}), \quad (12)$$

where $C_0 \triangleq \frac{2N_0 \mu_{g_0e_1}^2 k_p L}{\epsilon_0 \hbar \Omega_p}$. Here, N_0 represents the atomic density, ϵ_0 the vacuum permittivity, L the length of vapor cell, and k_p the wavenumber of probe laser.

C. An Open Problem

Equations (8), (10), and (12) characterize the microwave-to-optical conversion process of a multi-band RARE:

$$\{E_{s,n}\}_{n=1}^N \xrightarrow{(8)} \Omega \xrightarrow{(10)} \rho_{12} \xrightarrow{(12)} \mathcal{P}(\Omega). \quad (13)$$

The multi-band RF signals, $\{E_{s,n}\}$, are initially mapped onto the Rabi frequency vector Ω , which subsequently influences the quantum state ρ_{12} and is finally converted into the laser power, $\mathcal{P}(\Omega)$. This conversion enables the simultaneous detection of multiple RF bands from the laser power $\mathcal{P}(\Omega)$. However, the explicit mapping between the quantum state ρ_{12} and the Rabi frequency vector Ω necessitates solving the steady-state solution of the Lindblad master equation (10). While the solutions for single-band RAREs in the special case of $N = 1$ have been extensively studied [31], [32], the general case of multi-band RAREs with $N > 1$ has not yet been addressed in the literature. Instead, existing studies on multi-band RARE [20]–[26] primarily use experimental approaches to acquire the laser power $\mathcal{P}(\Omega)$ without solving the equation (10). In other words, the explicit transfer function from $\{E_{s,n}\}_{n=1}^N$ to $\mathcal{P}(\Omega)$ remains unknown, and its derivation forms the theme of the next section.

III. THEORETICAL FRAMEWORK OF MULTI-BAND RARE

This section presents a theoretical framework of multi-band RAREs. We first derive the steady-state solution of the Lindblad master equation in (10), taking into account multi-level electron transitions. Based on this solution, the transfer function of multi-band RAREs is subsequently obtained.

A. Solving the Lindblad Master Equation

To comprehend the electron transition behavior in Fig. 1, we first consider a dual-band system with $N = 2$ and then generalize our analysis to arbitrary multi-band systems. In particular, we focus on the steady-state solution of ρ_{12} , due to its direct correspondence with the measured probe laser, as in (12). The following theorem provides the closed-form expression for ρ_{12} in the case of $N = 2$.

Theorem 1. For $N = 2$, the steady-state solution of ρ_{12} to the Lindblad master equation in (10) is

$$\rho_{12} = j \frac{\rho_0(\Omega_1^2 + \Omega_2^2)}{(\Omega_1^2 + \Omega_2^2) + \Gamma^2}, \quad (14)$$

where $\rho_0 \triangleq \frac{\gamma_2 \Omega_p}{\gamma_2^2 + 2\Omega_p^2}$ and $\Gamma \triangleq \sqrt{\frac{2\Omega_p^2(\Omega_c^2 + \Omega_p^2)}{\gamma_2^2 + 2\Omega_p^2}}$.

Proof: The expression in (14) is derived by imposing the steady-state condition $\frac{\partial \rho}{\partial t} = 0$ and solving the linear equations governed by the Lindblad master equation (10), which comprises 25 variables corresponding to the density matrix elements. For brevity, the full derivation is omitted here, though the complete solutions for all elements of ρ , including ρ_{12} , are rigorously validated and provided in Appendix A for reproducibility. \square

Theorem 1 demonstrates that the coherence term ρ_{12} explicitly depends on the Rabi frequencies Ω_1 and Ω_2 of the dual-band signals, enabling the RARE to concurrently extract information from both frequency bands. Furthermore, the derived ρ_{12} expression for the *dual-band* RARE generalizes the prior *single-band* one given by [31], [32]

$$\rho_{12} = j \frac{\rho_0 \Omega_1^2}{\Omega_1^2 + \Gamma^2}. \quad (15)$$

Notably, setting $\Omega_2 = 0$ (or $\Omega_1 = 0$) in Theorem 1 recovers the single-band solution in (15), thereby validating the consistency of our generalized model.

Remark 1. (From dual-band to multi-band systems) Theorem 1 indicates that the quantum state, ρ_{12} , is determined by the sum square of Rabi frequencies, $\Omega_1^2 + \Omega_2^2$. Extending this result to an arbitrary N -band system, the steady-state solution of the coherence term ρ_{12} generalizes to

$$\rho_{12} = j \frac{\rho_0 \sum_{n=1}^N \Omega_n^2}{\sum_{n=1}^N \Omega_n^2 + \Gamma^2}, \quad (16)$$

where the dependence on $\sum_{n=1}^N \Omega_n^2$ reflects the collective contribution of all N frequency bands. This result is numerically validated in Section VI-B.

B. Transfer Function of Multi-band RAREs

1) *Transfer function at the IF band:* Building on the derived quantum state solution, we can now derive the transfer function of multi-band RAREs by following the mapping flow outlined in (13). To elaborate, substituting (16) into (12) yields the following explicit expression for the measured probe-laser power

$$\begin{aligned} y(t) &= \mathcal{P}(\Omega) = P_{\text{in}} \exp\left(-\frac{\chi_0 \sum_{n=1}^N \Omega_n^2}{\sum_{n=1}^N \Omega_n^2 + \Gamma^2}\right), \quad (17) \\ &= P_{\text{in}} \exp\left(-\frac{\chi_0 \sum_{n=1}^N |\Omega_{r,n} + \Omega_{s,n} e^{j(\delta_n t + \varphi_n)}|^2}{\sum_{n=1}^N |\Omega_{r,n} + \Omega_{s,n} e^{j(\delta_n t + \varphi_n)}|^2 + \Gamma^2}\right), \end{aligned}$$

where $\chi_0 \triangleq \rho_0 C_0$. This transfer function explicitly unveils the nonlinear relationship between the laser power and the sum-square of the multi-band signals. Such nonlinearity makes it challenging to decipher the data signals $E_{s,n}, \forall n$, especially their phase information. To overcome this challenge, the reference sources are typically placed in close proximity to the RARE, ensuring that the reference signal is orders of magnitude stronger than the data signal, e.g., $|E_{r,n}| \gg |E_{s,n}|$ and $\Omega_{r,n} \gg \Omega_{s,n}$ [33]. Under this strong-reference regime, the nonlinear transfer function in (17) can be accurately linearized via first-order Taylor expansion, greatly simplifying signal detection. Specifically, the derivative of $\mathcal{P}(\Omega)$ with respect to (w.r.t.) $\Omega_n, \forall n$ is expressed as:

$$\frac{\partial \mathcal{P}(\Omega)}{\partial \Omega_n} = \mathcal{P}(\Omega) \frac{2\chi_0 \Gamma^2 \Omega_n}{(\sum_{m=1}^N \Omega_m^2 + \Gamma^2)^2}. \quad (18)$$

Given (18), the linearized laser-power expression is presented in (19). It is observed that the resulting probe-laser power in (19) consists of three components: 1) a direct current (DC) bias, defined as $\mathcal{P}_r \triangleq \mathcal{P}(\Omega_r)$, resulting from the strong reference signal; 2) a band-specific gain factor, defined as $\kappa_n \triangleq \frac{\partial \mathcal{P}(\Omega_r)}{\partial \Omega_{r,n}} \frac{\mu_n}{h}$, quantifying the RARE's sensitivity for the n -th band; and 3) the modulated data signal, represented as $\text{Re}\{E_{s,n} e^{j(\delta_n t - \angle E_{r,n})}\}$, carrying the information payload. From (19), we can figure out the physical significance of a multi-band RARE.

Remark 2. (Physical significance of a multi-band RARE) A multi-band RARE operates as both a multi-band atomic mixer and a multi-band atomic amplifier, as illustrated in Fig. 2. The detection mechanism proceeds as follows:

- **Frequency mixing:** The data signal at each band ($\omega_n + \delta_n$) couples to the electron transition $|e_0\rangle \rightarrow |e_n\rangle$, inducing coherent down-conversion via the resonant frequency $\omega_{e_0 e_n} = \omega_n$. This generates an IF component at δ_n .

$$\mathcal{L} = \begin{bmatrix} \gamma_2 \rho_{22} + \sum_{i=4}^{N+3} \gamma_i \rho_{ii} & -\frac{\gamma_2}{2} \rho_{12} & -\frac{\gamma_3}{2} \rho_{13} & \cdots & -\frac{\gamma_{N+3}}{2} \rho_{1,N+3} \\ -\frac{\gamma_2}{2} \rho_{21} & \gamma_3 \rho_{33} - \gamma_2 \rho_{22} & -\frac{\gamma_{23}}{2} \rho_{23} & \cdots & -\frac{\gamma_{2,N+3}}{2} \rho_{2,N+3} \\ -\frac{\gamma_3}{2} \rho_{31} & -\frac{\gamma_{23}}{2} \rho_{32} & -\gamma_3 \rho_{33} & \cdots & -\frac{\gamma_{3,N+3}}{2} \rho_{3,N+3} \\ \vdots & \vdots & \vdots & \ddots & \vdots \\ -\frac{\gamma_{N+3}}{2} \rho_{N+3,1} & -\frac{\gamma_{2,N+3}}{2} \rho_{N+3,2} & -\frac{\gamma_{3,N+3}}{2} \rho_{N+3,3} & \cdots & -\gamma_{N+3} \rho_{N+3,N+3} \end{bmatrix}. \quad (11)$$

$$y(t) \approx \underbrace{\mathcal{P}(\Omega_r)}_{\text{DC bias}} + \sum_{n=1}^N \underbrace{\frac{\partial \mathcal{P}(\Omega_r)}{\partial \Omega_{r,n}} \frac{\mu_n}{\hbar}}_{\text{Gain for band } n} \underbrace{\text{Re}\{E_{s,n} e^{j(\delta_n t - \angle E_{r,n})}\}}_{\text{Data signal at band } n} \triangleq \mathcal{P}_r + \sum_{n=1}^N \kappa_n \text{Re}\{E_{s,n} e^{j(\delta_n t - \angle E_{r,n})}\}. \quad (19)$$

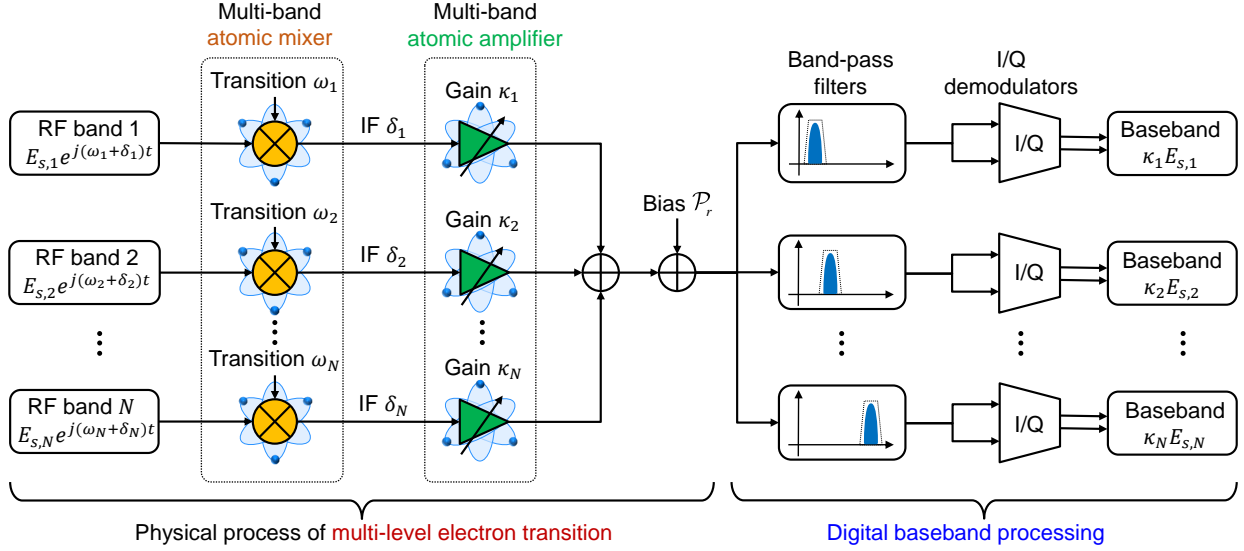


Figure 2. Equivalent signal transmission model of a multi-band RARE.

- **Amplification:** Each IF signal is amplified by the band-specific gain factor κ_n , which determines the RARE's sensitivity to the n -th RF band.
- **Signal aggregation:** The amplified IF components from all bands, together with the DC bias, superimpose in the probe-laser power $\mathcal{P}(\Omega)$, enabling simultaneous multi-band signal recovery.

2) *Transfer function at the digital baseband:* After obtaining the probe-laser power from the PD, digital baseband processing is conducted to convert the IF signal components into the digital baseband. To prevent inter-band interference, it is essential to make the IF components, $\text{Re}\{E_{s,n} e^{j(\delta_n t + \varphi_n)}\}$, mutually orthogonal. To this end, the separation between adjacent IFs, $\frac{\delta_{n+1} - \delta_n}{2}$, should exceed the average occupied bandwidth, $\frac{B_n + B_{n+1}}{2}$, by an adequate safe margin. For instance, we can set $N = 3$, $\delta_1 = 2\pi \times 100$ kHz, $\delta_2 = 2\pi \times 200$ kHz, $\delta_3 = 2\pi \times 300$ kHz, and $B_1 = B_2 = B_3 = 80$ kHz. Under this orthogonal condition, the data signal at each frequency band can be independently captured using band-pass filters and I/Q demodulators, as shown in the right part of Fig. 2. By further considering the system noise, the baseband signal originating from the n -th frequency band is thus obtained as

$$y_n = \kappa_n E_{s,n} + z_n, \quad \forall n \in \{1, 2, \dots, N\}. \quad (20)$$

Here, z_n denotes the noise, whose distribution will be discussed in next sub-section. The outputs $\{y_n\}$ enable multi-band CommunSense applications, as detailed in Section V.

C. Multi-Band Noise Characterization

In the final part of this section, we characterize the noise affecting the detected signal y_n by modifying the single-band

model [34]. Following [34], the noise, z_n , comprises two key components: *intrinsic noise* and *extrinsic noise*.

The intrinsic noise is largely attributed to the photon shot noise (PSN) of the PD [34]. The equivalent noise power across bandwidth B_n for band n is proportional to the DC bias of probe laser, \mathcal{P}_r , resulting from the multi-band reference signals as we derived in (19). Accordingly, it is derived as

$$\sigma_{i,n}^2 = \mathcal{P}_r B_n \hbar \omega_p \triangleq \mathcal{P}_r B_n C_1, \quad (21)$$

The extrinsic noise primarily arises from the black-body radiation at an ambient temperature T_a [34]. It contaminates the wireless data in the free space, and is thereby amplified by the gain of RARE. In the considered multi-band RARE system, the extrinsic noise model is based on modifying the amplified single-band gain factor adopted in [34] by the derived band-specific gain factor, κ_n . Then, the power of extrinsic noise at band n is derived as

$$\sigma_{E,n}^2 = \kappa_n^2 B_n \frac{4\hbar f_n^3 (e^{\hbar\omega_n/k_B T_a} + 1)}{\epsilon_0 c^3 (e^{\hbar\omega_n/k_B T_a} - 1)} \triangleq \kappa_n^2 B_n C_2, \quad (22)$$

where c the speed of light, ϵ_0 the dielectric constant, and k_B the Boltzmann constant.

Based on the preceding analysis, the noise, z_n , can be modeled as an additive white Gaussian noise obeying $z_n \sim \mathcal{CN}(0, \sigma_n^2)$, where

$$\sigma_n^2 = \sigma_{i,n}^2 + \sigma_{E,n}^2 = \mathcal{P}_r B_n C_1 + \kappa_n^2 B_n C_2. \quad (23)$$

IV. SENSITIVITY ANALYSIS AND MAXIMIZATION FOR MULTI-BAND RARES

In this section, we maximize the sensitivity of a multi-band RARE by optimizing the multi-band atomic amplifier through

the manipulation of the Rabi frequencies of reference signals. To this end, the explicit expression of the sensitivity is derived, analyzed, and then used to obtain the optimal Rabi frequencies.

A. Sensitivity Analysis

We utilize the Signal-to-Noise Ratio (SNR) of the baseband signal, y_n , to characterize the sensitivity of a multi-band RARE. For the n -th band, the SNR is given as

$$\text{SNR}_n = \frac{\kappa_n^2 |E_{s,n}|^2}{\kappa_n^2 B_n C_2 + \mathcal{P}_r B_n C_1} = \frac{|E_{s,n}|^2}{B_n C_2 + \frac{\mathcal{P}_r}{\kappa_n^2} B_n C_1}. \quad (24)$$

It is observed that SNR_n is monotonically increasing w.r.t. the parameter $\frac{\kappa_n^2}{\mathcal{P}_r}$. Note that both $\kappa_n = \frac{\partial \mathcal{P}(\Omega_r)}{\partial \Omega_{r,n}} \frac{\mu_n}{\hbar}$ and $\mathcal{P}_r = \mathcal{P}(\Omega_r)$ are affected by the Rabi frequency vector Ω_r of reference signals. Therefore, the sensitivity of RARE can be maximized by appropriately configuring the values of Ω_r through the transmission power control at the reference sources. Nevertheless, the multi-band gain factors, $\{\kappa_1, \kappa_2, \dots, \kappa_N\}$, of the multi-band atomic amplifier are coupled with each other due to their intricate dependence on all Rabi frequencies, as shown in (17) and (18). This coupling makes the maximization of SNR_n nonconvex and challenging. To address this issue, we propose a method to decouple the gain factor κ_n from the joint dependence on Ω_r , enabling tractable optimization.

1) *Decoupling of the gain factor κ_n* : The concepts of *Rabi sum-square* and *Rabi attentions* are introduced to decouple the gain factor κ_n .

Definition 1. (Rabi sum-square and Rabi attentions) We define the *Rabi sum-square* as the sum square of the Rabi frequencies of the reference signals, denoted as

$$\mathcal{A} \triangleq \sum_{n=1}^N \Omega_{r,n}^2. \quad (25)$$

Additionally, we introduce the variables, referred to as the *Rabi attention*, as

$$\alpha_n \triangleq \frac{\Omega_{r,n}^2}{\sum_{m=1}^N \Omega_{r,m}^2}, \forall n, \quad (26)$$

to characterize the ratio of $\Omega_{r,n}^2$ to the Rabi sum-square \mathcal{A} . The sum of all Rabi attentions equals 1 as $\sum_{n=1}^N \alpha_n = 1$.

One can observe that the optimization of the Rabi frequencies $\{\Omega_{r,1}, \Omega_{r,2}, \dots, \Omega_{r,N}\}$ is equivalent to the optimization of the Rabi sum-square and all Rabi attentions. This is attributed to the one-to-one mapping

$$\Omega_{r,n} = \sqrt{\mathcal{A} \alpha_n}, \forall n. \quad (27)$$

Utilizing this equivalence, the DC bias, \mathcal{P}_r , can be reformulated as a function of the Rabi sum-square:

$$\mathcal{P}_r = \mathcal{P}(\Omega_r) = P_{\text{in}} \exp\left(-\frac{\chi_0 \mathcal{A}}{\mathcal{A} + \Gamma^2}\right). \quad (28)$$

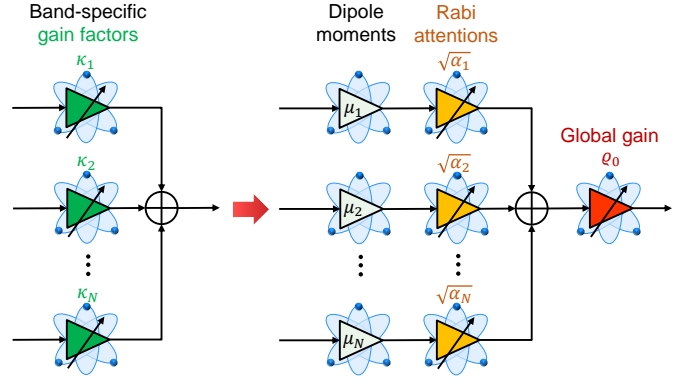


Figure 3. Decoupling of the multi-band atomic amplifier.

Moreover, the gain factor, κ_n , for band n can be recast as

$$\begin{aligned} \kappa_n &= \mathcal{P}_r \frac{2\chi_0 \Gamma^2 \Omega_{r,n}}{(\sum_{m=1}^N \Omega_{r,m}^2 + \Gamma^2)^2} \frac{\mu_n}{\hbar} = \mathcal{P}_r \frac{2\chi_0 \Gamma^2 \sqrt{\mathcal{A} \alpha_n}}{(\mathcal{A} + \Gamma^2)^2} \frac{\mu_n}{\hbar}, \\ &= \frac{2\chi_0 \Gamma^2}{\hbar} \mathcal{P}_r \frac{\sqrt{\mathcal{A}}}{(\mathcal{A} + \Gamma^2)^2} \sqrt{\alpha_n} \mu_n \triangleq \varrho_0 \sqrt{\alpha_n} \mu_n, \end{aligned} \quad (29)$$

where

$$\varrho_0 \triangleq \frac{2\chi_0 \Gamma^2}{\hbar} \mathcal{P}_r \frac{\sqrt{\mathcal{A}}}{(\mathcal{A} + \Gamma^2)^2}. \quad (30)$$

The relationship in (29) reveals that the gain factor for band n is composed of three parts: the transition dipole moment μ_n , the parameter ϱ_0 termed as the *global gain*, and the Rabi attention $\sqrt{\alpha_n}$. This structure allows for the decoupling of the multi-band atomic amplifier in Fig. 3, which is elaborated in Remark 3.

Remark 3. (Decoupled band-specific gain factors)

- **Global gain:** The global gain, ϱ_0 , depends solely on the Rabi sum-square, \mathcal{A} , which remains consistent across all frequency bands. This parameter determines the overall amplification gain, or equivalently the overall sensitivity, of the RARE to all frequency bands. Furthermore, the Rabi sum-square \mathcal{A} and Rabi attentions $\{\sqrt{\alpha_n}\}$ are independent variables, enabling decoupled optimization of the global gain and Rabi attentions.
- **Rabi attention:** The Rabi attentions, $\{\sqrt{\alpha_n}\}$, characterize how the RARE allocates its overall sensitivity to different frequency bands. This attention mechanism is a distinctive feature of the multi-band RARE introduced by the multi-level electron transition process. Increasing the proportion of $\Omega_{r,n}^2$ in the Rabi sum-square, \mathcal{A} , can enhance $\sqrt{\alpha_n}$, prioritizing sensitivity to the n -th band while proportionally reducing attention to others. This explains the experimentally observed sensitivity tradeoff of multi-band RAREs [25].
- **Transition dipole moment:** The transition dipole moments, $\{\mu_n\}$, are constants determined by the Rydberg atoms' inherent response to each frequency band. These parameters remain fixed, reflecting the fundamental

¹Without causing confusion, we will term both α_n and $\sqrt{\alpha_n}$ as the ‘‘Rabi attention’’ in subsequent discussions.

atomic properties rather than tunable operational settings.

As a result, the decoupling of band-specific gain factors allows us to *independently* optimize the global gain, ϱ_0 , and the Rabi attentions, $\{\sqrt{\alpha_n}\}$. This is instrumental in solving the sensitivity maximization problem.

2) *SNR analysis*: Following the decoupled κ_n in (29), the SNR at band n is reformulated as

$$\text{SNR}_n = \frac{\alpha_n \mu_n^2 |E_{s,n}|^2}{\alpha_n \mu_n^2 B_n C_2 + \frac{P_r}{\varrho_0^2} B_n C_1}. \quad (31)$$

Several insights can be drawn from (31). Firstly, the SNR is monotonically increasing w.r.t. the global gain normalized by the DC bias, $\frac{\varrho_0^2}{P_r}$. The normalization arises from the PSN, that is linearly related to P_r . Similar to the discussion in Remark 3, the normalized global gain, $\frac{\varrho_0^2}{P_r}$, serves as a global parameter dependent only on the Rabi sum-square. Increasing its value allows for a uniform enhancement of the SNRs across all frequency bands. Therefore, the maximization of all $\text{SNR}_n, \forall n$ is achieved only if $\frac{\varrho_0^2}{P_r}$ is maximized. Secondly, the Rabi attentions, $\alpha_n, \forall n$, dictate the RARE's emphasis on each frequency band. By increasing α_n , the RARE can amplify the signal, $E_{s,n}$, with a larger gain. However, this also results in an increase in the extrinsic noise, $\sigma_{E,n}^2$, within the same band.

B. Sensitivity Maximization

The optimal Rabi sum-square $\mathcal{A} = \sum_{n=1}^N \Omega_{r,n}^2$ is derived in the sequel to maximize the normalized global gain $\frac{\varrho_0^2}{P_r}$, thereby achieving the maximal sensitivity across all frequency bands. Notably, the optimization of the Rabi attentions $\{\alpha_n\}$ is contingent on application-specific performance metrics for CommunSense, which are detailed in Section V. To be specific, the sensitivity maximization problem is formulated as

$$\max_{\mathcal{A} > 0} \frac{\varrho_0^2}{P_r}, \quad (32)$$

where

$$\frac{\varrho_0^2}{P_r} = \frac{4\chi_0^2 \Gamma^4 P_{\text{in}}}{\hbar^2} \exp\left(-\frac{\chi_0 \mathcal{A}}{\mathcal{A} + \Gamma^2}\right) \frac{\mathcal{A}}{(\mathcal{A} + \Gamma^2)^4}. \quad (33)$$

The objective function in (33) comprises a constant, an exponential decay term, and a rational function of \mathcal{A} . Theorem 2 provides the closed-form global optimum for (32), which governs the fundamental sensitivity limits of the multi-band RARE.

Theorem 2. *The optimal \mathcal{A} that solves the problem in (32) is given as*

$$\mathcal{A}^* = \frac{\chi_0 + 4 - \sqrt{\chi_0^2 + 4\chi_0 + 16}}{\chi_0 - 4 + \sqrt{\chi_0^2 + 4\chi_0 + 16}} \Gamma^2. \quad (34)$$

Proof: (See Appendix B). \square

The function $\frac{\varrho_0^2}{P_r}$ is monotonically increasing for $\mathcal{A} < \mathcal{A}^*$ and monotonically decreasing for $\mathcal{A} > \mathcal{A}^*$. Utilizing Theorem 2, the normalized global gain $(\frac{\varrho_0}{P_r})^*$ that maximizes sensitivity is acquired. By substituting \mathcal{A}^* into (28) and (30), we can also

obtain the corresponding DC bias and global gain, denoted as P_r^* and ϱ_0^* respectively. Furthermore, Theorem 2 reveals that for a multi-band RARE, regardless the number of frequency bands considered, the sum square of the multi-band Rabi frequencies of the reference signals, $\mathcal{A} = \sum_{n=1}^N \Omega_{r,n}^2$, must be \mathcal{A}^* . Since $\Omega_{r,n} = \frac{\mu_n}{\hbar} |E_{r,n}|$ is proportional to the incident electric field, this optimal condition implies a fixed weighted sum of received reference-signal powers:

$$\sum_{n=1}^N \frac{\mu_n^2}{\hbar^2} |E_{r,n}|^2 = \text{constant}. \quad (35)$$

Nevertheless, while the Rabi sum-square is fixed, we can still control the distribution of Rabi frequencies $\left\{ \frac{\Omega_{r,n}^2}{\sum_{m=1}^N \Omega_{r,m}^2} \right\}$ to flexibly manipulate the Rabi attentions $\{\alpha_n\}$, thereby yielding degrees-of-freedom for further improving the CommunSense performance.

V. APPLICATIONS OF MULTI-BAND RARES

In this section, we apply multi-band RAREs to CommunSense scenarios. The optimal Rabi sum-square \mathcal{A}^* derived in Section IV-B is adopted, while the optimal Rabi attentions $\{\alpha_n\}$ for each CommunSense scenario are systematically designed. Our analysis establishes the performance limits for concurrent detection of the CommunSense information, $\{s_n\}$ in (4) and $\{d_n\}$ in (5), by RAREs.

A. Multi-Band Communications with RAREs

Consider the multi-band communication system. A single RARE is employed to capture information from N heterogeneous communication devices. Leveraging the derived transfer function of multi-band RARE with the maximal sensitivity, the received communication signal at band n is obtained as

$$y_n = \varrho_0^* \sqrt{\alpha_n} \mu_n h_n \sqrt{P_{t,n}} s_n + z_n. \quad (36)$$

Following this signal model, the multi-band symbols $\{s_n\}$ can be recovered through the maximum-likelihood (ML) detector:

$$\hat{s}_n = \arg \min_{s_n \in \mathbb{S}_n} \left\| \frac{y_n}{\varrho_0^* \sqrt{\alpha_n} \mu_n h_n \sqrt{P_{t,n}}} - s_n \right\|, \forall n, \quad (37)$$

To evaluate this multi-band communication system, we use the SE as the performance metric. Specifically, the formulated signal model allows us to explicitly express the SE as

$$\begin{aligned} \mathcal{C} &= \frac{\sum_{n=1}^N B_n \log_2(1 + \text{SNR}_n)}{\sum_{n=1}^N B_n}, \\ &= \sum_{n=1}^N \gamma_n \log_2 \left(1 + \frac{\alpha_n \mu_n^2 \varrho_0^{*2} |h_n|^2 P_{t,n}}{\alpha_n \mu_n^2 \varrho_0^{*2} B_n C_2 + P_r^* B_n C_1} \right), \end{aligned} \quad (38)$$

where $\gamma_n \triangleq \frac{B_n}{\sum_{m=1}^N B_m}$ denotes the proportion of bandwidth. For ease of discussion, the transmission power $P_{t,n}$ and bandwidth B_n are assumed to be fixed. We aim at maximizing the SE, \mathcal{C} , by optimizing Rabi attentions, $\{\alpha_n\}$, under the constraints $\sum_{n=1}^N \alpha_n = 1$ and $\alpha_n \geq 0, \forall n$, to approach the

performance limit of multi-band RAREs. Let $\beta_n \triangleq \frac{|h_n|^2 P_{t,n}}{B_n C_2}$ and $\epsilon_n \triangleq \frac{\mathcal{P}_r^* C_1}{\mu_n^2 \varrho_0^2 C_2}$, simplifying the problem to:

$$\max_{\{\alpha_n\}_{n=1}^N} \sum_{n=1}^N \gamma_n \log_2 \left(1 + \frac{\beta_n \alpha_n}{\alpha_n + \epsilon_n} \right), \quad (39)$$

$$\text{s.t.} \quad \sum_{n=1}^N \alpha_n = 1, \quad (39a)$$

$$\alpha_n \geq 0, \forall n. \quad (39b)$$

To obtain the global optimal solution for Rabi attentions, the concavity of problem (39) is proved as follows: 1) *Constraints*: The constraints $\sum_{n=1}^N \alpha_n = 1$ and $\alpha_n \geq 0$ are clearly convex. 2) *Objective function*: The second derivative of \mathcal{C} w.r.t. α_n is

$$\frac{\partial^2 \mathcal{C}}{\partial \alpha_n^2} = -\log_2 \frac{\gamma_n \beta_n \epsilon_n (2(1+\beta_n)\alpha_n + (2+\beta_n)\epsilon_n)}{(\alpha_n + \epsilon_n)^2 ((1+\beta_n)\alpha_n + \epsilon_n)^2} < 0, \quad (40)$$

and $\frac{\partial^2 \mathcal{C}}{\partial \alpha_n \partial \alpha_m} = 0, \forall n \neq m$, such that the Hessian matrix is diagonal with negative entries, confirming concavity. Therefore, the global optimal Rabi attentions can be attained by solving Karush-Kuhn-Tucker (KKT) conditions, as presented in Theorem 3 [35].

Theorem 3. *The optimal Rabi attentions, $\alpha_n, \forall n \in \{1, 2, \dots, N\}$, that solve problem (39) satisfy*

$$\alpha_n^* = \left(\frac{-(2+\beta_n)\epsilon_n + \sqrt{\beta_n^2 \epsilon_n^2 + 4\nu^* \gamma_n \beta_n (1+\beta_n)\epsilon_n}}{2(1+\beta_n)} \right)^+, \quad (41)$$

where $(x)^+ \triangleq \max(0, x)$, and the non-negative Lagrange multiplier ν^* is properly selected to ensure $\sum_{n=1}^N \alpha_n^* = 1$.

Proof: (See Appendix C). \square

Combining Theorem 2 and Theorem 3 yields the optimal design of Rabi frequencies of the reference signals: $\Omega_{r,n}^* = \sqrt{\mathcal{A}^* \alpha_n^*}$, where \mathcal{A}^* (Theorem 2) ensures maximal sensitivity, and α_n^* (Theorem 3) optimizes SE. This joint optimization enables the multi-band RARE to achieve the maximal capacity in concurrent multi-band communications.

It needs to be emphasized the metric of SE is just one possible criterion for multi-band RAREs. Many other metrics could also be considered, such as energy efficiency, user fairness, and secure communication rate. These metrics will result in different optimal Rabi attentions, while the optimal Rabi sum-square can be kept as (34) because its design is independent of the specific metrics.

B. Multi-Band Sensing with RAREs

Multi-band RAREs can enable multi-granularity wireless sensing by exploiting the frequency-dependent phase sensitivity of multi-band signals. In this scenario, our objective is to recover the displacements, $\{d_n\}$, of all sensing targets from the received signal, $\{y_n\}$, formulated as

$$y_n = \varrho_0^* \sqrt{\alpha_n} \mu_n h_n \sqrt{P_{t,n}} e^{j \frac{\omega_n}{c} d_n} + z_n. \quad (42)$$

To this end, we use the ML detector to estimate d_n as

$$\hat{d}_n = \frac{c}{\omega_n} \angle \left(\frac{y_n}{\varrho_0^* \sqrt{\alpha_n} \mu_n h_n \sqrt{P_{t,n}}} \right), \forall n. \quad (43)$$

The sensing accuracy of \hat{d}_n can be assessed using the NCLRB, defined as the CRLB of d_n normalized by the variance of d_n . The NCLRB offers a theoretical lower bound of the normalized mean square error when estimating d_n . To be specific, we assume d_n a uniform distribution, $d_n \sim \mathcal{U}[-\frac{\pi c}{\omega_n}, \frac{\pi c}{\omega_n}]$, yielding $\mathbb{E}(|d_n|^2) = \frac{\pi^2 c^2}{3\omega_n^2}$. Following the derived signal model in (42), the NCRLB of d_n is formulated as

$$\begin{aligned} \text{NCRLB}(d_n) &= \frac{\text{CRLB}(d_n)}{\mathbb{E}(|d_n|^2)} = \frac{1}{\mathbb{E}(|d_n|^2)} \frac{c^2}{\omega_n^2} \frac{1}{2\text{SNR}_n}, \quad (44) \\ &= \frac{3B_n C_2}{2\pi^2 |h_n|^2 P_{t,n}} + \frac{3\mathcal{P}_r^* B_n C_1}{2\pi^2 \alpha_n \mu_n^2 \varrho_0^2 |h_n|^2 P_{t,n}}. \end{aligned}$$

The sum of all NCRLBs is adopted as a performance metric to evaluate the overall sensing error, which is minimized by optimizing the Rabi attentions. The notation $\xi_n \triangleq \frac{3\mathcal{P}_r^* B_n C_1}{2\pi^2 \mu_n^2 \varrho_0^2 |h_n|^2 P_{t,n}}$ is introduced to simplify the expression of the formulated problem as

$$\min_{\{\alpha_n\}_{n=1}^N} \sum_{n=1}^N \frac{\xi_n}{\alpha_n}, \quad (45)$$

$$\text{s.t.} \quad \sum_{n=1}^N \alpha_n = 1, \quad (45a)$$

$$\alpha_n \geq 0, \forall n. \quad (45b)$$

The term $\frac{3B_n C_2}{2\pi^2 |h_n|^2 P_{t,n}}$ in $\text{NCRLB}(d_n)$ is omitted in problem (45) as it is irrelevant to α_n . This optimization problem is shown to be convex, and its global optimal solution can be readily derived by solving KKT conditions as

$$\alpha_n^* = \frac{\sqrt{\xi_n}}{\sum_{m=1}^N \sqrt{\xi_m}}. \quad (46)$$

As a result, by configuring the Rabi frequencies as $\Omega_{r,n}^* = \sqrt{\mathcal{A}^* \alpha_n^*}$ using the optimal Rabi sum-square in Theorem 2 and the optimal Rabi attentions in (46), the maximal sensing accuracy averaged over multiple frequency bands is achieved.

VI. EXPERIMENTAL RESULTS

In this section, we present numerical experiments to verify the effectiveness of multi-band RARE.

A. Experimental Setup

The default experimental settings for the RARE are as follows unless specified otherwise. We consider a dual-band wireless system with $N = 2$, where sub-6G and mmWave signals are detected by a single RARE. Cesium atoms are stored in a vapor cell with a length of $L = 2$ cm, which has an atomic density of $N_0 = 4.89 \times 10^{10} \text{ cm}^{-3}$. The probe laser having a wavelength of 852.94 nm and an input power of 120 μW excites the atoms from the ground state $|g_0\rangle = 6S_{1/2}$ to the lowly excited state $|g_1\rangle = 6P_{3/2}$. The coupling laser, with a wavelength of 509.49 nm and a power of 17 mW, further triggers the atoms from $6P_{3/2}$ to the initial Rydberg state $|e_0\rangle = 60D_{5/2}$. The Rabi frequencies of the probe and coupling lasers are fixed as $2\pi \times 5.7$ MHz and $2\pi \times 0.97$ MHz, respectively. The two final Rydberg states are configured as $|e_1\rangle = 61P_{3/2}$, and $|e_2\rangle = 62P_{3/2}$.

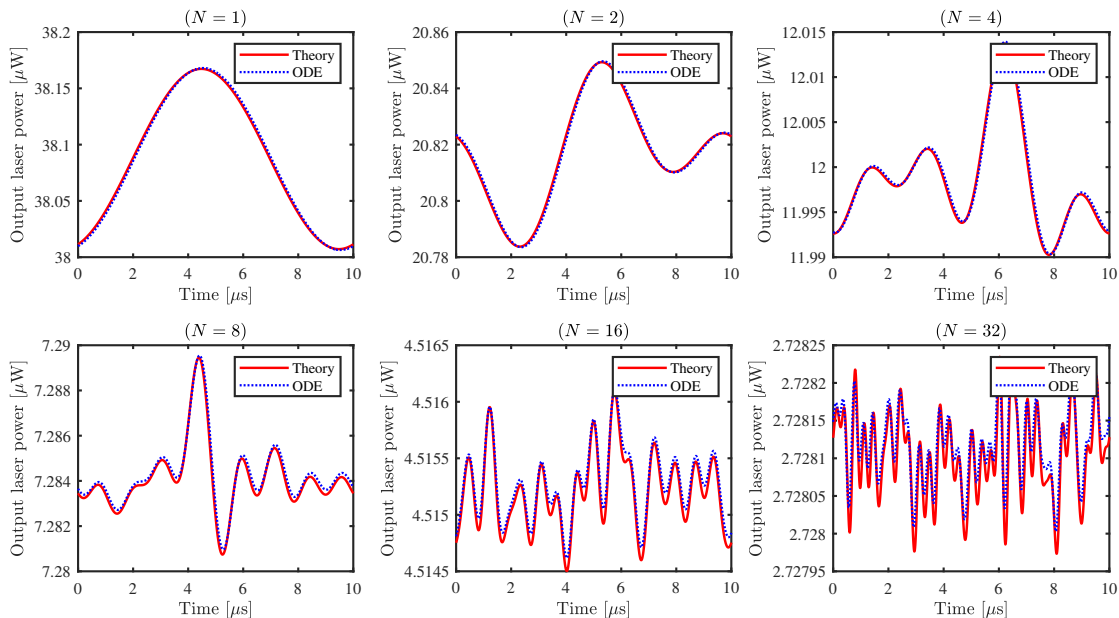


Figure 4. Waveforms of multi-band RAREs for $N = 1, 2, 4, 8, 16, 32$.

The electron transition $61P_{3/2} \rightarrow 62P_{3/2}$ resonates with the sub-6G signal operating at $\omega_{e_0e_1} = 2\pi \times 3.212\text{GHz}$ and the transition $61P_{3/2} \rightarrow 63P_{3/2}$ resonates with the mmWave signal operating at $\omega_{e_0e_2} = 2\pi \times 30.628\text{GHz}$. The corresponding transition dipole moments are calculated as $\mu_{g_0g_1} = 2.586qa_0$, $\mu_{g_1e_0} = 0.013qa_0$, $\mu_1 = 2410qa_0$, and $\mu_2 = 736.452qa_0$, respectively, where $q = 1.602 \times 10^{-19}\text{C}$ denotes the unit charge and $a_0 = 52.9\text{pm}$ the Bohr radius [36]. The decay rate γ_2 is $2\pi \times 5.2\text{MHz}$. The ambient temperature is $T_a = 290\text{K}$. Using these parameters, the optimal Rabi sum-square is calculated as $\sqrt{\mathcal{A}^*} = 2\pi \times 0.586\text{MHz}$.

Furthermore, The configurations for the wireless signals are as follows. The frequencies of reference signals are tuned resonant with the electron transition frequencies, $\omega_1 = \omega_{e_0e_1} = 2\pi \times 3.212\text{GHz}$ and $\omega_2 = \omega_{e_0e_2} = 2\pi \times 30.628\text{GHz}$. The IFs and occupied bandwidths of the dual-band signals are set as $\delta_1 = 2\pi \times 100\text{kHz}$, $B_1 = 80\text{kHz}$ and $\delta_2 = 2\pi \times 200\text{kHz}$, $B_2 = 80\text{kHz}$. The transmission power of the two wireless data sources are configured as 20 dBm. The wireless channel fading is assumed to be -90dB .

For comparison, two classic receivers operating at $\omega_1 = 2\pi \times 3.212\text{GHz}$ and $\omega_2 = 2\pi \times 30.628\text{GHz}$ are deployed in the same wireless environment to detect the dual-band signal, which serve as the performance benchmarks. They are denoted as “CR1” for the sub-6G band and “CR2” for the mmWave band. Each of them is equipped with a single half-wavelength dipole antenna and a front-end circuit dedicated for each band. Their specific configurations are the same as the existing literature [16]. For example, the antenna gains and low-noise-amplifier (LNA) gains are set as 2.1 dB and 30 dB, and the equivalent LNA noise temperature is 100 Kelvin.

B. Validation of Signal Transmission Model

To validate the effectiveness of our derived signal model, we present Fig. 4 to illustrate the alignment of waveforms between the signal model acquired in (19), labeled as “Theory”, and the exact solution, labeled as “ODE”. Here, the exact solution is numerically computed by using the ordinary differential equation (ODE) solver, (e.g., the fourth-order Runge-Kutta method), to address the Lindblad master equation given in (10). The number of frequency bands are set as $N = \{1, 2, 4, 8, 16, 32\}$. A time window of 10 μs is selected to observe the waveforms, during which the amplitude of wireless signals for each band remains constant. The Rabi frequencies of reference signals are fixed as $\Omega_{l,n} = 2\pi \times 1\text{MHz}, \forall n$, while the Rabi frequencies of data signals are randomly generated from the distribution $\Omega_{s,n} \sim 2\pi \times \mathcal{U}(0\text{kHz}, 1\text{kHz})$. Thereby, the strong reference signal condition, $|\Omega_{r,n}| \gg |\Omega_{s,n}|, \forall n$, is satisfied. The IFs for each frequency band are selected as $\delta_n/2\pi = 100n\text{kHz}, \forall n \in \{1, 2, \dots, N\}$. It is observed from Fig. 4 that the derived waveforms align well with the exact solutions for the cases $N = 1, 2, 4, 8$, validating the efficacy of our signal model. However, when $N = 16$ or $N = 32$, the theoretical waveforms slightly deviate from the exact solutions. This derivation stems from the narrow instantaneous bandwidth of a RARE [37]. Specifically, when N is small, the maximum IF (e.g., $\delta_8/2\pi = 800\text{kHz}$ for $N = 8$) is within the maximum instantaneous bandwidth of a RARE (typically $1 \sim 10\text{MHz}$ [37]). In this context, the quantum state ρ_{12} will have adequate time to converge to the steady-state solution derived in (16). On the contrary, as N increases, the maximum IF (e.g., $\delta_{32}/2\pi = 3.2\text{MHz}$) gradually approaches the maximum instantaneous bandwidth of a RARE, resulting in insufficient time for the electron transition to reach a steady state. This discrepancy causes the

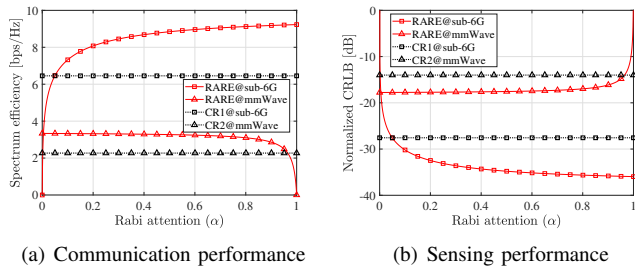


Figure 5. CommunSense performance at different frequency bands for different settings of Rabi attention, α .

exact solution to deviate from the theoretical model. Overall, the derived signal transmission model precisely captures the dynamics of multi-level electron transitions when the signal bandwidth falls within the detectable instantaneous bandwidth of a RARE.

C. Performance of Multi-Band RAREs

In this subsection, we evaluate multi-band CommunSense performance by comparing the multi-band RARE with a classic sub-6G receiver, CR1, and a classic mmWave receiver, CR2. The communication performance is quantified by the SE while the sensing performance is assessed using the NCRLB.

Fig. 5 evaluates the CommunSense performance under varying Rabi attentions. Specifically, the Rabi attentions for the two bands are expressed as $\alpha_1 = \alpha$ and $\alpha_2 = 1 - \alpha$, with α ranging from 0 to 1. As observed in Fig. 5, the CommunSense performance at the sub-6G band achieved by the multi-band RARE continuously improves with increasing α , whereas the performance at the mmWave band consistently declines. This is attributed to the attention mechanism of the multi-band RARE, where α characterizes the proportion of sensitivity allocated to the sub-6G band. Notably, when $\alpha = 1$, the multi-band RARE simplifies to the existing single-band RARE. In this case, the CommunSense performance at the sub-6G band is maximized, yielding an SE of 9.2 bps/Hz and an NCRLB of -36 dB. However, the CommunSense services at the mmWave band are broken. Conversely, setting $\alpha = 0.5$ results in a negligible degradation in the sub-6G performance (a 0.4 bps/Hz reduction in SE and 1.2 dB increase in NCRLB), while the mmWave band experiences a significant improvement, with the SE increasing from 0 bps/Hz to 3.5 bps/Hz and the NCRLB reducing from infinity to -18 dB. This example demonstrates the superiority of multi-band RARE over single-band RARE in addressing heterogeneous CommunSense tasks. Furthermore, the multi-band RARE achieves a remarkable CommunSense performance gain compared to the two classic receivers, provided that the Rabi attention is appropriately configured. For instance, when $\alpha = 0.4$, there is an average increase of 2 bps/Hz in SE and a 5 dB decrease in NCRLB. It is noteworthy that all these multi-band CommunSense performance gains are achieved within a single RARE device.

Then, we evaluate the effects of Rabi sum-square on the achieved SE in Fig. 6(a) and on the NCRLB in Fig. 6(b), both averaged on the two frequency bands. In addition to the performance achieved by two classic receivers, denoted

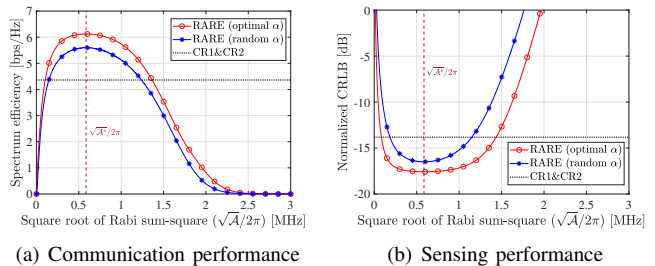


Figure 6. Performance comparison between the multi-band RAREs and classic receivers for different settings of Rabi sum-square, \mathcal{A} .

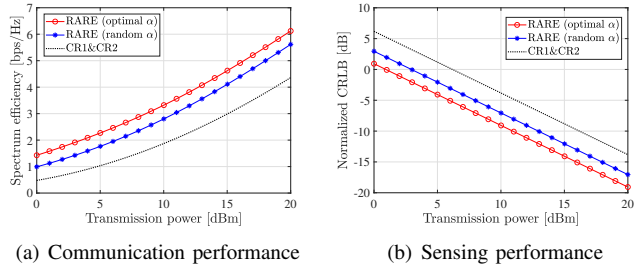


Figure 7. Performance comparison between the multi-band RAREs and classic receivers for different settings of the transmission power, $P_{t,n}$.

as “CR1&CR2”, we also include the multi-band RARE with randomly sampled Rabi attentions, $\alpha \sim \mathcal{U}(0, 0.5)$, as a benchmark. As the Rabi sum-square \mathcal{A} increases, the performance of RAREs initially improves, but then declines. This trade-off can be interpreted by the electron transition process. Specifically, when Rabi frequency of the reference signal is either small or large, all electrons are predominantly located in either the initial Rydberg state or final Rydberg state. In both of these scenarios, the Rydberg atom is unable to effectively respond to the weak wireless data signal. Sensitivity to the weak signal is achieved only when the Rabi frequency of the reference signal is moderate enough for approximately half of the electrons to be situated in the final Rydberg state. Nevertheless, the derived optimal Rabi sum-square, $\sqrt{\mathcal{A}^*} = 2\pi \times 0.586$ MHz, can consistently capture the most sensitive state of a RARE, regardless of the values of Rabi attentions or the conducted CommunSense services. This is due to the fact that the Rabi sum-square only influences the global gain, ϱ_0 , amplified on all frequency bands, thereby uniformly enhancing the sensitivity of a RARE to all frequency bands. Using the optimal Rabi sum-square and Rabi attentions, a RARE can outperform classic receivers by 2 bps/Hz in SE and by 5 dB in NCRLB. This verifies the necessity for the optimization of Rabi sum-square to maximize the sensitivity.

Finally, Fig. 7 illustrates the CommunSense performance as a function of the transmission power, $P_{t,n}$, spanning from 0 dBm to 20 dBm. The optimal Rabi sum-square is adopted for both “RARE (optimal α)” and “RARE (random α)”. As depicted in Fig. 7, the multi-band RAREs significantly outperform classic receivers in all considered transmission power. Furthermore, compared to the benchmark of “RARE (random α)”, the optimal design of Rabi attentions further improves the SE by 0.5 bps/Hz and reduces the NCRLB by 2 dB. This result underscores the critical importance of

optimizing Rabi attentions for each communication or sensing task.

VII. CONCLUSIONS

In this paper, we have mathematically characterized the underlying physical mechanisms of multi-band RAREs. In particular, the transfer function of multi-band RAREs has been derived by solving the closed-form expression for the quantum response of Rydberg atoms excited by multi-band RF signals. Our analysis reveals that a multi-band RARE functions as both a multi-band atomic mixer and a multi-band atomic amplifier. Additionally, the attention mechanism of the multi-band atomic amplifier has been discovered. We have also presented optimal design for the atomic amplifier to maximize the receiver sensitivity and the overall CommunSense performance.

We conclude this paper by outlining potential avenues for future research. To begin with, the current derivation assumes that the frequency of each band resonates with the corresponding electron transition. However, understanding the quantum response of multi-band RAREs under *off-resonant* conditions remains an open problem. Moreover, leveraging the multi-band capability to protect data privacy is a promising direction. Finally, the multi-band RARE can be incorporated with the atomic multiple-input-multiple-output (MIMO) technique [9], [38] to further improve wireless CommunSense performance.

APPENDIX

A. Steady-state solutions of ρ

The steady-state solutions of ρ to the equation (10) when $N = 2$ are given as

$$\begin{aligned}\rho_{11} &= \frac{(\Omega_p^2 + \gamma_2^2)(\Omega_1^2 + \Omega_2^2) + \Omega_c^2 \Omega_p^2}{(\gamma_2^2 + 2\Omega_p^2)(\Omega_1^2 + \Omega_2^2) + 2\Omega_p^2(\Omega_c^2 + \Omega_p^2)}, \\ \rho_{12} &= j \frac{\gamma_2 \Omega_p (\Omega_1^2 + \Omega_2^2)}{(\gamma_2^2 + 2\Omega_p^2)(\Omega_1^2 + \Omega_2^2) + 2\Omega_p^2(\Omega_c^2 + \Omega_p^2)}, \\ \rho_{13} &= - \frac{\Omega_c \Omega_p^3}{(\gamma_2^2 + 2\Omega_p^2)(\Omega_1^2 + \Omega_2^2) + 2\Omega_p^2(\Omega_c^2 + \Omega_p^2)}, \\ \rho_{14} &= -j \frac{\gamma_2 \Omega_1 \Omega_c \Omega_p}{(\gamma_2^2 + 2\Omega_p^2)(\Omega_1^2 + \Omega_2^2) + 2\Omega_p^2(\Omega_c^2 + \Omega_p^2)}, \\ \rho_{15} &= -j \frac{\gamma_2 \Omega_2 \Omega_c \Omega_p}{(\gamma_2^2 + 2\Omega_p^2)(\Omega_1^2 + \Omega_2^2) + 2\Omega_p^2(\Omega_c^2 + \Omega_p^2)}, \\ \rho_{22} &= \frac{\Omega_p^2 (\Omega_1^2 + \Omega_2^2)}{(\gamma_2^2 + 2\Omega_p^2)(\Omega_1^2 + \Omega_2^2) + 2\Omega_p^2(\Omega_c^2 + \Omega_p^2)}, \\ \rho_{24} &= - \frac{\Omega_1 \Omega_c \Omega_p^2}{(\gamma_2^2 + 2\Omega_p^2)(\Omega_1^2 + \Omega_2^2) + 2\Omega_p^2(\Omega_c^2 + \Omega_p^2)}, \\ \rho_{25} &= - \frac{\Omega_2 \Omega_c \Omega_p^2}{(\gamma_2^2 + 2\Omega_p^2)(\Omega_1^2 + \Omega_2^2) + 2\Omega_p^2(\Omega_c^2 + \Omega_p^2)}, \\ \rho_{33} &= \frac{\Omega_p^4}{(\gamma_2^2 + 2\Omega_p^2)(\Omega_1^2 + \Omega_2^2) + 2\Omega_p^2(\Omega_c^2 + \Omega_p^2)},\end{aligned}$$

$$\begin{aligned}\rho_{44} &= \frac{\Omega_1^2 \Omega_p^2 (\Omega_p^2 + \Omega_c^2)}{(\gamma_2^2 + 2\Omega_p^2)(\Omega_1^2 + \Omega_2^2)^2 + 2\Omega_p^2(\Omega_c^2 + \Omega_p^2)(\Omega_1^2 + \Omega_2^2)}, \\ \rho_{45} &= \frac{\Omega_1 \Omega_2 \Omega_p^2 (\Omega_p^2 + \Omega_c^2)}{(\gamma_2^2 + 2\Omega_p^2)(\Omega_1^2 + \Omega_2^2)^2 + 2\Omega_p^2(\Omega_c^2 + \Omega_p^2)(\Omega_1^2 + \Omega_2^2)}, \\ \rho_{55} &= \frac{\Omega_2^2 \Omega_p^2 (\Omega_p^2 + \Omega_c^2)}{(\gamma_2^2 + 2\Omega_p^2)(\Omega_1^2 + \Omega_2^2)^2 + 2\Omega_p^2(\Omega_c^2 + \Omega_p^2)(\Omega_1^2 + \Omega_2^2)}, \\ \rho_{23} &= \rho_{34} = \rho_{35} = 0.\end{aligned}$$

For the elements, ρ_{mn} with $m > n$, they can be obtained as $\rho_{mn} = \rho_{nm}^*$ since the matrix ρ is Hermitian.

B. Proof of Theorem 2

Problem (32) is equivalent to maximizing the function $f(\mathcal{A}) = \exp\left(-\frac{\chi_0 \mathcal{A}}{\mathcal{A} + \Gamma^2}\right) \frac{\mathcal{A}}{(\mathcal{A} + \Gamma^2)^4}$ with $\mathcal{A} > 0$. To solve it, we introduce the variable transformation $x = \frac{\mathcal{A}}{\mathcal{A} + \Gamma^2}$. Then, we get $0 \leq x < 1$ and $\mathcal{A} = \frac{x}{1-x} \Gamma^2$. The function $f(\mathcal{A})$ can thus be rewritten as

$$f(\mathcal{A}) = \frac{1}{\Gamma^6} e^{-\chi_0 x} x (1-x)^3 \triangleq g(x). \quad (47)$$

The gradient of $g(x)$ is given as

$$\frac{dg(x)}{dx} = \frac{1}{\Gamma^6} e^{-\chi_0 x} (1-x^2) (\chi_0 x^2 - (\chi_0 + 4)x + 1). \quad (48)$$

By setting $\frac{dg(x)}{dx} = 0$ and doing some tedious calculations, we can obtain the optimal x that maximizes $g(x)$ in the range $x \in [0, 1)$ as

$$x^* = \frac{\chi_0 + 4 - \sqrt{\chi_0^2 + 4\chi_0 + 16}}{2\chi_0}. \quad (49)$$

When $0 \leq x < x^*$, the gradient $\frac{dg(x)}{dx}$ is greater than 0 and thus $g(x)$ monotonically increases, while when $x^* < x < 1$, the gradient $\frac{dg(x)}{dx}$ is smaller than 0 and thus $g(x)$ monotonically decreases,

By further invoking the relationship $\mathcal{A} = \frac{x}{1-x} \Gamma^2$. The optimal Rabi sum-square is thus given as

$$\mathcal{A}^* = \frac{\chi_0 + 4 - \sqrt{\chi_0^2 + 4\chi_0 + 16}}{\chi_0 - 4 + \sqrt{\chi_0^2 + 4\chi_0 + 16}} \Gamma^2. \quad (50)$$

This completes the proof.

C. Proof of Theorem 3

The Lagrange function of problem (39) is given as

$$\mathcal{L} = \sum_{n=1}^N \gamma_n \log_2 \left(1 + \frac{\beta_n \alpha_n}{\alpha_n + \epsilon_n} \right) + \frac{1}{\nu} \left(1 - \sum_{n=1}^N \alpha_n \right). \quad (51)$$

Here, ν is the Lagrange multiplier and we adopt its reciprocal form $1/\nu$ for ease of later expression. The KKT conditions are given as

$$\frac{\partial \mathcal{L}}{\partial \alpha_n} = \frac{\gamma_n \beta_n \epsilon_n}{((1 + \beta_n) \alpha_n + \epsilon_n)(\alpha_n + \epsilon_n)} - \frac{1}{\nu} = 0, \forall n, \quad (52)$$

$$\sum_{n=1}^N \alpha_n = 1. \quad (53)$$

The condition in (52) follows a quadratic form. As $\alpha_n \geq 0$, we have $\frac{\gamma_n \beta_n \epsilon_n}{((1+\beta_n)\alpha_n + \epsilon_n)(\alpha_n + \epsilon_n)} > 0$. Therefore, the Lagrange multiplier ν must be greater than 0 as well. Otherwise there will be no feasible solutions to (52) for all n . Given $\nu \geq 0$, the solutions of these quadratic equations should obey

$$\alpha_n = \frac{-(2 + \beta_n)\epsilon_n \pm \sqrt{\beta_n^2 \epsilon_n^2 + 4\nu\gamma_n\beta_n(1 + \beta_n)\epsilon_n}}{2(1 + \beta_n)}. \quad (54)$$

By further considering the requirement $\alpha_n \geq 0$, the solution of $\frac{-(2+\beta_n)\epsilon_n - \sqrt{\beta_n^2 \epsilon_n^2 + 4\nu\gamma_n\beta_n(1+\beta_n)\epsilon_n}}{2(1+\beta_n)}$ should be discarded as it is always smaller than 0 for all n . Besides, the other one needs to be modified as

$$\alpha_n^* = \left(\frac{-(2 + \beta_n)\epsilon_n + \sqrt{\beta_n^2 \epsilon_n^2 + 4\nu^*\gamma_n\beta_n(1 + \beta_n)\epsilon_n}}{2(1 + \beta_n)} \right)^+, \quad (55)$$

where $(x)^+ \triangleq \max(0, x)$. The optimal Lagrange multiplier ν^* is properly selected to satisfy the constraint $\sum_{n=1}^N \alpha_n^* = 1$. This completes the proof.

REFERENCES

- [1] B. Liu, L. Zhang, Z. Liu, Z. Deng, D. Ding, B. Shi, and G. Guo, "Electric field measurement and application based on Rydberg atoms," *Electromagn. Sci.*, vol. 1, no. 2, pp. 1–16, Jun. 2023.
- [2] M. Cui, Q. Zeng, and K. Huang, "Rydberg atomic receiver: Next frontier of wireless communications," *arXiv preprint arXiv:2412.12485*, Dec. 2024.
- [3] S. S. A. Yuan, X. Y. I. Xu, J. Yuan, G. Xie, C. Huang, X. Chen, Z. Huang, and W. E. I. Sha, "Electromagnetic modeling and capacity analysis of Rydberg atom-based MIMO system," *IEEE Antennas Wireless Propag. Lett.*, pp. 1–5, 2025.
- [4] C. T. Fancher, D. R. Scherer, M. C. S. John, and B. L. S. Marlow, "Rydberg atom electric field sensors for communications and sensing," *IEEE Trans. Quantum Eng.*, vol. 2, no. 3501313, pp. 1–13, Mar. 2021.
- [5] Y. Chen, X. Guo, C. Yuen, Y. Zhao, Y. Guan, C. M. S. See, M. Debbah, and L. Hanzo, "Harnessing Rydberg atomic receivers: From quantum physics to wireless communications," *arXiv preprint arXiv:2501.11842*, Jan. 2025.
- [6] G. Gao, M. Chen, H. Feng, Z. Zhu, A. Chen, Z. Wu, T. Mao, W. Dai, P. Peng, and D. Zheng, "Rydberg communication antennas with self-decoupling for dynamic radar interference based on heterodyne technology," *Appl. Phys. Lett.*, vol. 126, no. 13, p. 134002, Apr. 2025.
- [7] H. Zhang, Y. Ma, K. Liao, W. Yang, Z. Liu, D. Ding, H. Yan, W. Li, and L. Zhang, "Rydberg atom electric field sensing for metrology, communication and hybrid quantum systems," *Sci. Bull.*, vol. 69, no. 10, pp. 1515–1535, May 2024.
- [8] F. Zhang, B. Jin, Z. Lan, Z. Chang, D. Zhang, Y. Jiao, M. Shi, and J. Xiong, "Quantum wireless sensing: Principle, design and implementation," in *Proc. Annu. Int. Conf. Mobile Comput. Netw. (ACM MobiCom'23)*, Oct. 2023, pp. 1–15.
- [9] M. Cui, Q. Zeng, and K. Huang, "Towards atomic MIMO receivers," *IEEE J. Sel. Areas Commun.*, vol. 43, no. 3, pp. 659–673, Jan. 2025.
- [10] M. Cui, Q. Zeng, Z. Wang, and K. Huang, "Realizing quantum wireless sensing without extra reference sources: Architecture, algorithm, and sensitivity maximization," *arXiv preprint arXiv:2504.21234*, Apr. 2025.
- [11] B. Xu, J. Zhang, Z. Chen, B. Cheng, Z. Liu, Y.-C. Wu, and B. Ai, "Channel estimation for Rydberg atomic receivers," *arXiv preprint arXiv:2503.08985*, Mar. 2025.
- [12] H. Kim, H. Park, and S. Kim, "Quantum-MUSIC: Multiple signal classification for quantum wireless sensing," *IEEE Wireless Commun. Lett.*, 2025.
- [13] H. Wu, X. Yao, C. Xie, K.-D. Wu, S. Wu, R. Ni, G.-Y. Xiang, and C. Gong, "On-off keying signal detection based on hidden markov model for Rydberg atomic sensor," *IEEE Trans. Commun.*, 2025.
- [14] Z. Liu, L. Zhang, B. Liu, Z. Zhang, G. Guo, D. Ding, and B. Shi, "Deep learning enhanced Rydberg multifrequency microwave recognition," *Nat. Commun.*, vol. 13, no. 1, p. 1997, Apr. 2022.
- [15] H. Nyquist, "Thermal agitation of electric charge in conductors," *Phys. Rev.*, vol. 32, no. 1, pp. 110–113, Jul. 1928.
- [16] T. Gong, J. Sun, C. Yuen, G. Hu, Y. Zhao, Y. Guan, C. M. S. See, M. Debbah, and L. Hanzo, "Rydberg atomic quantum receivers for classical wireless communications and sensing: Their models and performance," *arXiv preprint arXiv:2412.05554*, Dec. 2024.
- [17] T. Gong, A. Chandra, C. Yuen, Y. L. Guan, R. Dumke, C. M. S. See, M. Debbah, and L. Hanzo, "Rydberg atomic quantum receivers for classical wireless communication and sensing," *IEEE Wireless Commun.*, pp. 1–11, 2025.
- [18] L. J. Chu, "Physical limitations of omni-directional antennas," *J. Appl. Phys.*, vol. 19, no. 12, pp. 1163–1175, Dec. 1948.
- [19] S. Aboagye, M. Amin Saeidi, H. Tabassum, Y. Tayyar, E. Hossain, H.-C. Yang, and M.-S. Alouini, "Multi-band wireless communication networks: Fundamentals, challenges, and resource allocation," *IEEE Trans. Commun.*, vol. 72, no. 7, pp. 4333–4383, Jul. 2024.
- [20] C. Holloway, M. Simons, A. H. Haddab, J. A. Gordon, D. A. Anderson, G. Raithel, and S. Voran, "A multiple-band Rydberg atom-based receiver: AM/FM stereo reception," *IEEE Antennas Propag. Mag.*, vol. 63, no. 3, pp. 63–76, Jun. 2021.
- [21] Y. Du, N. Cong, X. Wei, X. Zhang, W. Luo, J. He, and R. Yang, "Realization of multiband communications using different Rydberg final states," *AIP Adv.*, vol. 12, no. 6, p. 065118, Jun. 2022.
- [22] D. H. Meyer, J. C. Hill, P. D. Kunz, and K. C. Cox, "Simultaneous multiband demodulation using a Rydberg atomic sensor," *Phys. Rev. Appl.*, vol. 19, p. 014025, Jan. 2023.
- [23] L.-H. Zhang, B. Liu, Z.-K. Liu, Z.-Y. Zhang, S.-Y. Shao, Q.-F. Wang, Y. Ma, T.-Y. Han, G.-C. Guo, D.-S. Ding, and B.-S. Shi, "Ultra-wide dual-band rydberg atomic receiver based on space division multiplexing radio-frequency chip modules," *Chip*, vol. 3, no. 2, p. 100089, Jun. 2024.
- [24] G. Allinson, M. J. Jamieson, A. R. Mackellar, L. Downes, C. S. Adams, and K. J. Weatherill, "Simultaneous multiband radio-frequency detection using high-orbital-angular-momentum states in a Rydberg-atom receiver," *Phys. Rev. Res.*, vol. 6, p. 023317, Jun. 2024.
- [25] S. You, M. Cai, H. Zhang, Z. Xu, and H. Liu, "Exclusive effect in Rydberg atom-based multi-band microwave communication," *Photonics*, vol. 10, no. 3, Mar. 2023.
- [26] W. Wen, S. Yan, R. Wang, X. Li, J. Tan, X. Pang, W. Zhai, W. Cui, and Y. Gao, "Rydberg-atom-based multiband frequency-hopping communication receiver using five-level atomic system," *Opt. Express*, vol. 32, no. 24, pp. 42 872–42 884, Nov. 2024.
- [27] H. Kim, H. Park, J. Won, and S. Kim, "Multi-band quantum wireless sensing for Rydberg atomic receivers," *IEEE Commun. Lett.*, 2025.
- [28] S. Parkvall, E. Dahlman, A. Furuskar, and M. Frenne, "NR: The new 5G radio access technology," *IEEE Commun. Standards Mag.*, vol. 1, no. 4, pp. 24–30, Dec. 2017.
- [29] M. S. Sim, Y.-G. Lim, S. H. Park, L. Dai, and C.-B. Chae, "Deep learning-based mmWave beam selection for 5G NR/6G with sub-6 GHz channel information: Algorithms and prototype validation," *IEEE Access*, vol. 8, pp. 51 634–51 646, 2020.
- [30] C. J. Foot, *Atomic Physics*. Oxford University Press, 2005.
- [31] M. Jing, Y. H. Hu, J. Ma, H. Zhang, L. Zhang, L. Xiao, and S. Jia, "Atomic superheterodyne receiver based on microwave-dressed Rydberg spectroscopy," *Nat. Phys.*, vol. 1, pp. 911–915, Jun. 2020.
- [32] X.-H. Liu, K.-Y. Liao, Z.-X. Zhang, H.-T. Tu, W. Bian, Z.-Q. Li, S.-Y. Zheng, H.-H. Li, W. Huang, H. Yan, and S.-L. Zhu, "Continuous-frequency microwave heterodyne detection in an atomic vapor cell," *Phys. Rev. Appl.*, vol. 18, no. 5, p. 054003, Nov. 2022.
- [33] C. L. Holloway, M. T. Simons, J. A. Gordon, and D. Novotny, "Detecting and receiving phase-modulated signals with a Rydberg atom-based receiver," *IEEE Antennas Wireless Propag. Lett.*, vol. 18, no. 9, pp. 1853–1857, Sep. 2019.
- [34] H.-T. Tu, K.-Y. Liao, H.-L. Wang, Y.-F. Zhu, S.-Y. Qiu, H. Jiang, W. Huang, W. Bian, H. Yan, and S.-L. Zhu, "Approaching the standard quantum limit of a Rydberg-atom microwave electrometer," *Sci. Adv.*, vol. 10, no. 51, p. eads0683, 2024.
- [35] S. Boyd and L. Vandenberghe, *Convex Optimization*. Cambridge University Press, 2004.
- [36] N. Šibalić, J. Pritchard, C. Adams, and K. Weatherill, "ARC: An open-source library for calculating properties of alkali Rydberg atoms," *Comput. Phys. Commun.*, vol. 220, pp. 319–331, Nov. 2017.
- [37] Z. Jia, Q. Li, Y. Wang, Y. You, B. Chen, and Y. Peng, "Properties and utilization in time-dependent Rydberg EIT," *Opt. Continuum*, vol. 3, no. 2, pp. 135–147, Feb. 2024.
- [38] M. Cui, Q. Zeng, and K. Huang, "MIMO precoding for Rydberg atomic receivers," *arXiv preprint arXiv:2408.14366*, Aug. 2024.